Ceramics International 50 (2024) 17063–17074

Contents lists available at ScienceDirect

Ceramics International

journal homepage: www.elsevier.com/locate/ceramint

Synthesis, structural, photoluminescence, and EPR analysis of far red emitting $Ca_3La_2W_2O_{12}:Mn^{4+}$ inorganic phosphor for applications in plant-growth LEDs

Jung-Kul Lee [a], Amol Nande [b], Aadil Ahmad Bhat [a], S. Watanabe [c], T.K. Gundu Rao [c], Vijay Singh [a,*]

[a] Department of Chemical Engineering, Konkuk University, Seoul, 05029, South Korea
[b] Guru Nanak College of Science, Ballarpur, 442701, India
[c] Institute of Physics, University of Sao Paulo, SP, 05508-090, Brazil

ARTICLE INFO

Handling editor: P. Vincenzini

Keywords:
EPR
Mn^{4+}
$Ca_3La_2W_2O_{12}$
Luminescence

ABSTRACT

This study explores the structural and optical properties of Mn^{4+} doped $Ca_3La_2W_2O_{12}$ phosphor. It also investigates the incorporation of Mn^{4+} ions for deep red emission and electron paramagnetic resonance (EPR) analysis. The phosphors were synthesized using the sol-gel method, and their properties were thoroughly examined using a combination of X-ray diffraction (XRD), Fourier transform infrared (FT-IR), photoluminescence (PL), and EPR technique. The XRD analysis provided insights into the phase purity, and constituents of the synthesized samples. Under 345 nm excitation, we observed far red emission at 705 nm, with the highest emission intensity occurring at a concentration of 0.0025 mol of Mn^{4+} metal ions in the host matrix. Concentration quenching was observed due to dipole-quadrupole interactions. The CIE chromaticity coordinates confirm far red region emission, and the estimated correlated color temperature (CCT) suggests that these phosphors can be used for bright illumination. Concurrently, the EPR examination also confirmed the presence of Mn^{4+} ions in the host matrix and showed the effect of variation on Mn^{4+} concentration in the EPR spectroscopy measurements. Furthermore, the electron paramagnetic resonance analysis demonstrated a distinctive six-line spectrum with a *g*-factor of approximately 1.98, indicating the presence of paramagnetic Mn^{4+} ions. This primary line was accompanied by a broader resonance with a linewidth of 950 Gauss, partially overlapping the six-line spectrum. The initial investigation indicates that this far red emitting phosphor can be applied to plant-growth LEDs.

1. Introduction

Luminescent materials including inorganic and organic phosphors with excellent photoluminescent properties are widely used for several applied applications such as light-emitting diodes (LEDs), displays, medical, and photocatalytic applications [1–4]. Inorganic phosphors have long been at the forefront of materials research, owing to their diverse range of applications in optoelectronic devices, lighting technologies, and information displays. These materials exhibit exceptional luminescent properties, enabling them to efficiently convert energy from various sources into visible light. The design and development of novel inorganic phosphors are pivotal in advancing the performance and efficiency of a wide array of devices, including LEDs, cathode-ray tube displays, and X-ray detectors [3,4]. Inorganic phosphors are already used as a next-generation white source due to their energy-saving ability, efficiency, long lifetime, and controlled size as well as they are environmentally friendly [5,6].

In recent times, researchers have expanded their focus to encompass not only the applications of inorganic phosphors in white light LED's but also the utilization of LED's for indoor plant cultivation [7,8]. Indoor plant cultivation can explore new fields in the agriculture industry. Indoor plant cultivation allows us to grow plants in a controlled and pollution-free environment. It also protects the plants from bad weather like floods, and droughts gaining high productivity in growing vegetables, fruits, and crops. Thus, indoor cultivation helps to open a solution to the global food problem as well as providing a new opportunity for researchers to work more on it.

The previous works suggest that blue light (400–500 nm), red light

* Corresponding author.
E-mail address: vijayjiin2006@yahoo.com (V. Singh).

https://doi.org/10.1016/j.ceramint.2024.02.183
Received 30 December 2023; Received in revised form 4 February 2024; Accepted 14 February 2024
Available online 19 February 2024
0272-8842/© 2024 Elsevier Ltd and Techna Group S.r.l. All rights reserved.

(620–690 nm), and far red light (700–740 nm) play vital roles in photosynthesis, phototropism, and photomorphogenesis reactions [7, 9–11]. The red light has been observed to have a beneficial impact on plant growth, specifically concerning the development of plant stem nodes and the regulation of plant height. Additionally, it plays a vital role in accelerating the synthesis of sugars and carbohydrates, as well as facilitating the assimilation of nitrogen. Consequently, the deployment of high-quality LEDs tailored for plant growth becomes a vital requirement to enhance productivity in indoor cultivation settings. Mn^{4+} doped inorganic phosphors show emission in the region of the far red which is suitable for higher value vegetables. Mn^{4+} is a transition metal ion and has $3d^3$ electronic configurations. These metal ions can retain their oxidation states when utilized as dopants to substitute cations within octahedral geometries. Moreover, these phosphors are blue-light-excitable phosphors which give emission in far red region from 630 nm to 730 nm [8,12,13]. In this context, LED lighting systems derived from these materials serve as a highly advantageous illumination source for indoor plant cultivation.

Far red region is utilized in plant cultivation, optical thermometry, food analysis, and medical imaging [14–17]. The range of 700 nm–740 nm in far red light aligns closely with the absorption spectra of phytochrome, which is crucial for plant development. This suggests that it can be employed to control plant growth [18]. Consequently, plant growth lights can be produced by combining near-infrared phosphors with LED chips [19]. Understanding and manipulating specific light wavelengths, notably dep red light in artificial systems, empower growers to create tailored environments that enhance growth stages, optimize photosynthesis, and regulate flowering and fruiting for healthier crops and improved yields. In view of theses, several phosphors with exceptional performance have been reported by researchers in recent years, including $Ca_3Al_{12}Ge_3O_{12}:Eu^{3+}$ (far red phosphor) [20], and $SrMgAl_{10-y}Ga_yO_{17}:Mn^{4+}$ (red phosphor) [21], $Gd_2ZnTiO_6:Mn^{4+}$ (red phosphor) [22], $Gd_2ZnTiO_6:Mn^{4+}$, Yb^{3+} (far red phosphor) [23], La_2LiSbO_6: Mn^{4+}, Mg^{2+} (far red phosphor) [24], among others.

Notably, it has been observed that Mn^{4+} ions find facile stabilization within hexagonal octahedral host matrices. The inherent hexagonal geometry of tungstates, recognized for their affordability and ease of synthesis, further underscores their suitability. Additionally, these materials demonstrate exceptional chemical and physical stability, while their magnetic and optical properties are highly commendable. In the domain of inorganic phosphors, numerous researchers have favored tungstates as their host materials, employing rare-earth and transition metals as dopants to harness their luminescent potential. Tang et al. [25] synthesized Eu^{3+} doped alkali rare-earth double tungstate nanoparticles using hydrothermal reaction method. The phosphors have high rendering index and good correlated color temperature (CCT) value suggesting a promising candidate for red-emitting component of indoor lightings. Yang et al. [26] studied Sm^{3+}-doped $CaGdSbWO_8$ phosphors which were synthesized using high-temperature solid state reaction methods. The samples showed good emission in the red region and pursued good thermal stability. Among the vast landscape of phosphors, $Ca_3La_2W_2O_{12}$, a complex oxide, has gained significant attention due to its intriguing optical properties. $Ca_3La_2W_2O_{12}$ is a promising candidate for deep red emission, making it desirable for applications where high-efficiency red phosphors are essential, such as in full-color displays, optical communications, and biological imaging. The addition of dopant ions to the $Ca_3La_2W_2O_{12}$ lattice can enhance its luminescent properties, expanding its potential applications in advanced technologies. Li et al. [27] synthesized and studied Tm^{3+}-doped $Ca_3La_2W_2O_{12}$ using high temperature solid state reaction method. The synthesized samples showed application in plant cultivation. Lovisa et al. [28] synthesized Eu doped $SrMo_{0.5}WO_4$ phosphors using microwave-hydrothermal method. The phosphor showed red emission attributed to $^5D_0 \rightarrow {}^7F_2$ transition of Eu^{3+} ions suggesting the samples may be used in solid-state lightning devices. Zang et al. [29] synthesized Eu^{3+} doped bismuth lanthanum tungstate phosphors using solid state reaction method. The synthesized phosphors had good thermal stability and showed the potential application for white light emitting diodes. Huang et al. [7] investigated Mn^{4+}-doped $Ca_3La_2W_2O_{12}$ phosphors, which were synthesized using the high-temperature solid-state reaction method. Their study provided compelling evidence for the appropriateness of these phosphors in the context of indoor plant cultivation. Wu et al. [30] also employed the high-temperature solid-state reaction approach to synthesize Mn^{4+}-doped $Ca_3La_2W_2O_{12}$ phosphors. Their findings concurred with the potential of these phosphors and suggested their strong candidacy for the development of specialized light-emitting diodes (LEDs) aimed at promoting comprehensive plant growth enhancements. To our knowledge, there has been a limited electron paramagnetic resonance (EPR) investigation on this system. However, it can offer valuable insights into the electronic properties of semiconductors, ceramics, and other materials. Mn^{4+} is a non-rare earth dopant element with $3d^3$ electronic configuration which shows emission in far red region. The ion replaces various metal ions like W^{6+}, Sn^{4+}, Al^{3+}, Ge^{4+}, Ta^{5+} and Ti^{4+} from the host crystal structures. The emission of Mn^{4+} generally observe due to the $^2E \rightarrow {}^4A_2$ spin and parity forbidden transition. The peak positions depend on the host matrix of the samples. The Mn^{4+} activated phosphors show prominent excitation peaks in the 300–600 nm range. Under the excitation of near ultra-violet or blue light the Mn^{4+} doped phosphors exhibit emission in the far red region which is an ideal requirement for LEDs in artificial plant cultivations.

In the presented work, $Ca_3La_2W_2O_{12}:xMn^{4+}$ (x = 0.0012, 0.0025, 0.005, 0.01, 0.02, 0.03, 0.04, and 0.06) red phosphors were synthesized using sol-gel method. This manuscript presents a detailed study of the synthesized phosphors, with a particular focus on Mn^{4+} doping, to understand their structural, optical, and EPR spectroscopic properties. The synthesis of these materials through the sol-gel method offers precise control over their composition and crystalline structure, enabling the tailoring of their properties for specific applications. This study uses a variety of analytical methods, such as X-ray diffraction, Fourier transform infrared (FT-IR), photoluminescence (PL), and EPR techniques, to gain a comprehensive understanding of the material. Additionally, the study includes simulated EPR spectra of $Ca_3La_2W_2O_{12}$ phosphor with Mn^{4+} ions.

2. Materials and method

2.1. Synthesis of $Ca_3La_2W_2O_{12}:xMn^{4+}$

A series of samples with the empirical formula $Ca_3La_2W_2O_{12}:xMn^{4+}$ (x = 0.0012, 0.0025, 0.005, 0.01, 0.02, 0.03, 0.04, and 0.06) were prepared using the sol-gel method. The sol-gel method is ideal for synthesizing phosphors, as it allows for precise control over the composition, purity, and structure of the final products. The starting materials were $Ca(NO_3)_2{\bullet}4H_2O$, $La(NO_3)_3{\bullet}6H_2O$, $(NH_4)_6W_{12}O_{39}{\bullet}xH_2O$, $Mn(NO_3)_2{\bullet}4H_2O$, and citric acid ($C_6H_8O_7$). It is important to note that all the starting materials used in this study were of analytical grade and were used without any additional purification. In the synthesis of these samples, a constant concentration ratio of $C_6H_8O_7$ to metal ions was maintained at 3:1 to ensure reproducibility. The study aimed to investigate the influence of Mn^{4+} in the synthesized series, leading to the preparation of eight distinct samples of $Ca_3La_2W_2O_{12}:xMn^{4+}$, each with varying concentrations.

The synthesis process for the phosphors is visually depicted in Fig. 1. To produce $Ca_3La_2W_2O_{12}:xMn^{4+}$, a series of steps were followed. Initially, all the precursor materials were dissolved in 10 ml of deionized (DI) water, and the resulting solution was stirred for 60 min with a magnetic stirrer until it became a transparent aqueous solution. Subsequently, this transparent aqueous solution was subjected to a drying process at 110 °C for a duration of 12 h in an oven. This drying step led to the formation of porous solid matrices, often referred to as xerogels. The xerogels were heated at 400 °C for 2 h, resulting in a black residual product. The final products were then obtained by annealing

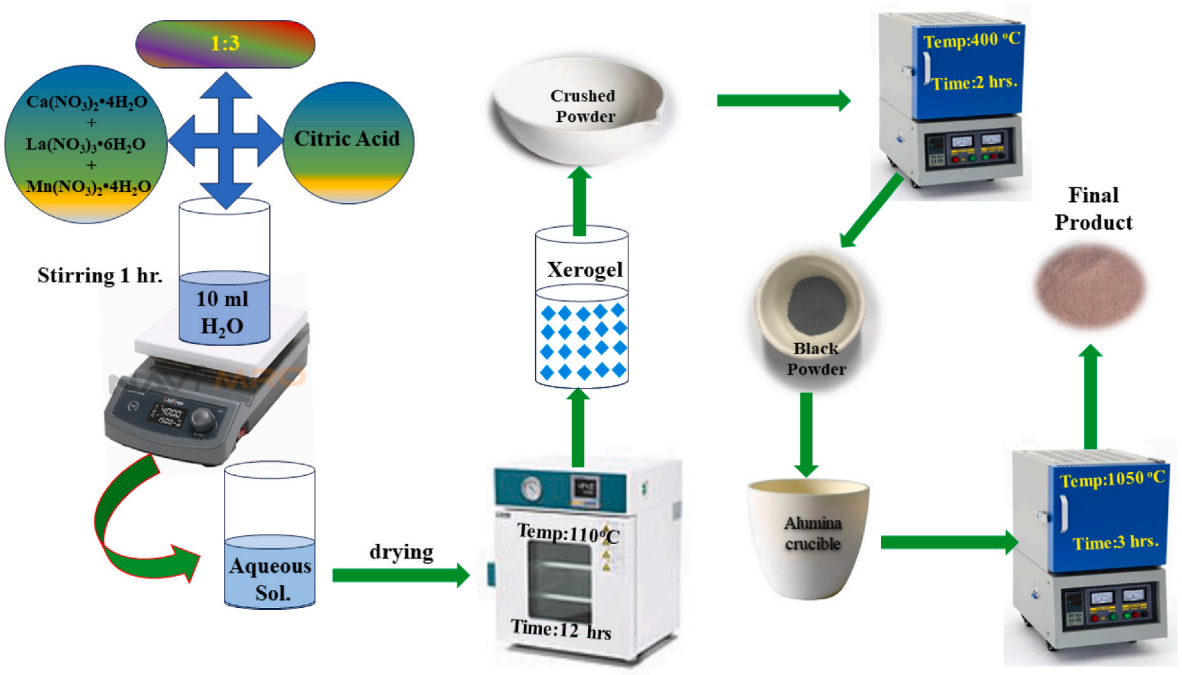

Fig. 1. Schematic diagram of the synthesis process used for preparing the samples.

the black residual products at 1050 °C for 3 h. The samples were ground into a fine powder using a mortar and pestle and then used for further characterization.

2.2. Measurements and characterization

The series of samples were sent to Rigaku X-ray diffractometer for obtaining X-ray diffraction (XRD) patterns of the samples using the Cu-Kα radiation (λ = 1.5406 Å). The obtained XRD patterns are used for the structure determination of the samples. The phase identification of the host materials was done using Joint Committee on Powder Diffraction Standards (JCPDS) file. The Fourier transform infrared (FT-IR) spectra was performed with Thermo-Nicolet equipment in the range of 400–4000 cm^{-1}. UV-VIS-NIR measurement was carried out at room temperature on a Cary 5000 Spectrophotometer. Photoluminescence measurements were carried out at room temperature on a Shimadzu RF-5301PC, spectrofluorophotometer equipped with Xenon flash lamp. The EPR spectra of the sample were recorded on a JEOL FE1X ESR

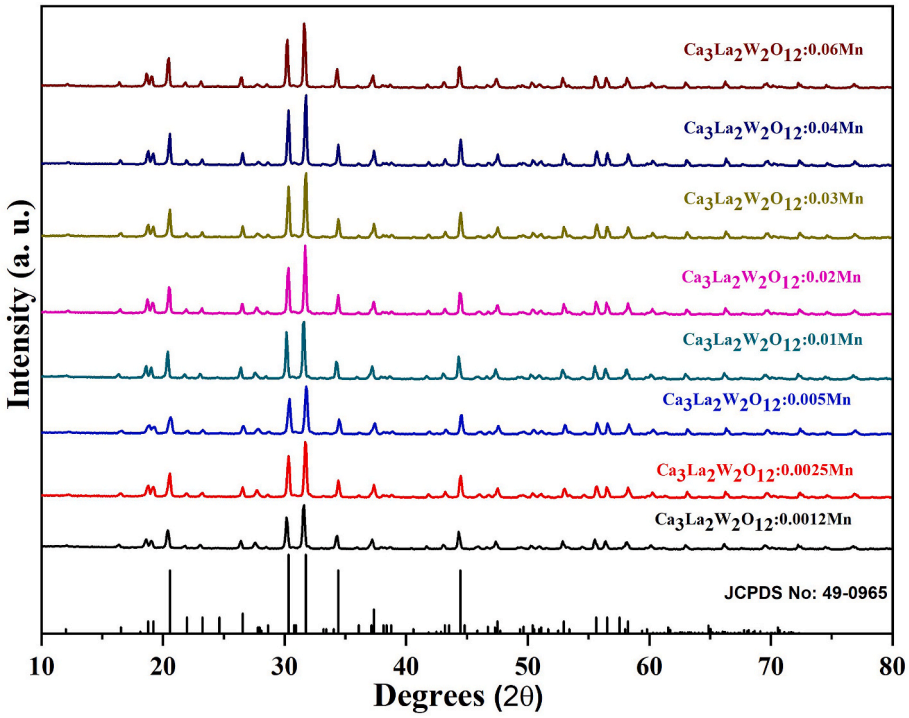

Fig. 2. XRD patterns of the $Ca_3La_2W_2O_{12}$:xMn^{4+} (*x*: 0.0012–0.06) phosphor along with standard data.

Spectrometer, operating in the X-band frequencies, with a field modulation of 100 kHz.

3. Results and discussion

3.1. X-ray diffraction studies

Fig. 2 illustrates the X-ray diffraction (XRD) patterns for the $Ca_3La_2W_2O_{12}$:$x$$Mn^{4+}$ phosphors, alongside the reference data sourced from the JCPDS. The observed XRD peaks in all synthesized phosphors exhibit a remarkable agreement with the standard JCPDS file No. 49–0965. Importantly, no indications of impurity phases or extraneous crystalline structures were discernible in the diffraction patterns, affirming the high purity and phase homogeneity of the synthesized materials. The rigorous matching of the JCPDS dataset with the obtained XRD data strongly supports the categorization of the current samples as hexagonal in crystal system. These samples confirm to the $R\bar{3}m$ space group, with unit cell parameters a = b = 9.754 nm and c = 55.460 nm, revealing the structural integrity and consistency within the set. Furthermore, a close analysis of the XRD results indicates a subtle but discernible shift in the position of diffraction peaks towards higher values. This phenomenon is typically observed when smaller metal ions effectively replace larger metal ions within the lattice, reflecting changes in the crystal structure due to the ionic substitution process. The notable shift is in line with our measurements, confirming the successful incorporation of Mn^{4+} ions into the lattice structure. It is most likely that the Mn^{4+} ion (ionic radius 0.53 Å) prefers to substitute W^{6+} ions in $Ca_3La_2W_2O_{12}$, as the ionic radius of W^{6+} (0.6 Å) is close to that of Mn^{4+} (0.53 Å). Moreover, it is noteworthy that the intensity of the prominent diffraction peak centered at 31.73° displays a proportional increase with the escalating concentration of Mn^{4+} metal ions. This intensity variation directly correlates with the concentration of Mn^{4+} dopant ions, substantiating their presence and confirming the impact on the crystal structure, which plays a pivotal role in the luminescent properties of the phosphor [31].

In the context of $Ca_3La_2W_2O_{12}$:$x$$Mn^{4+}$ phosphors, the shift in the 2θ angle observed in X-ray diffraction (XRD) patterns can have a significant impact on the estimated crystallite size. The relationship between the 2θ angle and crystallite size is described by the Scherrer equation.

$$D = 0.9\lambda/\beta\mathrm{Cos}\theta \quad (1)$$

D represents the crystallite size, k is the shape factor (typically assumed to be 0.9), λ denotes the X-ray wavelength, β is the full width at half-maximum (FWHM) of the diffraction peak, θ is the diffraction angle [32–34]. The Average crystallite size and micro strain of the samples are presented in Table 1. In the case of the $Ca_3La_2W_2O_{12}$:$x$$Mn^{4+}$ phosphors, a shift in the 2θ angle to a higher value (i.e., moving to the right in the XRD pattern) indicates a reduction in the d-spacing of the crystal lattice planes. This reduction corresponds to a more compact and smaller crystalline structure. Therefore, as the 2θ angle shifts to higher values, it suggests a decrease in crystallite size within the material. The shift in the 2θ angle in the XRD patterns of $Ca_3La_2W_2O_{12}$:$x$$Mn^{4+}$ phosphors is inversely proportional to the estimated crystallite size. Analyzing this shift provides valuable insights into changes in the structural properties of the phosphors, particularly with respect to crystallite size variations.

Table 1
Represents the average crystallite size and lattice strain.

S. No.	Sample Composition	Crystallite Size (nm)	Lattice Strain
1	$Ca_3La_2W_2O_{12}$:0.0012Mn	35.94	0.0037
2	$Ca_3La_2W_2O_{12}$:0.0025Mn	35.95	0.0037
3	$Ca_3La_2W_2O_{12}$:0.005Mn	34.51	0.0038
4	$Ca_3La_2W_2O_{12}$:0.01Mn	41.07	0.0032
5	$Ca_3La_2W_2O_{12}$:0.02Mn	40.93	0.0032
6	$Ca_3La_2W_2O_{12}$:0.03Mn	41.10	0.0032
7	$Ca_3La_2W_2O_{12}$:0.04Mn	43.15	0.0031
8	$Ca_3La_2W_2O_{12}$:0.06Mn	43.13	0.0031

3.2. FT-IR studies

The FT-IR spectrum gives important information about the material's composition and chemical bonding. The positions of absorption bands depend on the compound's crystal structure and environment. FT-IR spectrum of $Ca_3La_2W_2O_{12}$:0.0025Mn^{4+} phosphor was recorded in the wavelength range of 400–4000 cm^{-1}. In Fig. 3, the FT-IR spectrum of the phosphor $Ca_3La_2W_2O_{12}$:0.0025Mn^{4+} is presented. Fig. 3 clearly shows vibrations at 462, 586, 666, 840, 1106, 2309, 2983, and 3424 cm^{-1} and fluctuations near at 1220 and 3551 cm^{-1}. In the lower wavenumber region (400-800 cm^{-1}), we observe a series of peaks related to the lattice vibrations of the crystal structure. The exact positions and intensities of these bands depend on the crystal symmetry and the specific atomic arrangements in Mn doped $Ca_3La_2W_2O_{12}$. Tungsten oxide compounds typically have characteristic absorption bands in the 700-1000 cm^{-1} range [35]. These bands are associated with W–O stretching vibrations and can provide information about the bonding environment of tungsten in the material. The bands near 666 and 840 cm^{-1} are due to stretching and bending vibrations for O–W–O or W–*O*–W in WO_3 [36,37]. Also, band at 666 cm^{-1} can also be due to LaO stretching [38] and 462 cm^{-1} can be attributed to CaO vibrations [39].

The band at 1598 cm^{-1} corresponds to a stretching or bending vibration involving oxygen atoms in the crystal lattice. It might be associated with metal-oxygen bonds (La–O, W–O) or the symmetric stretching of oxygen atoms in the lattice. Inorganic materials often exhibit strong absorption bands in the 3000-4000 cm^{-1} range due to the stretching vibrations of O–H bonds. In the mid-infrared region, stretching vibrations are associated with Ca–O, La–O, and W–O bonds. The positions and intensities of these bands will depend on the specific coordination environment of these metals in the crystal structure. The band at 3439 cm^{-1} is likely associated with O–H stretching vibrations [40,41]. It could arise from residual water or hydroxyl groups in the sample. The other peaks were observed due to the residuals left from starting chemicals. The presence of manganese ions could introduce additional absorption bands in the spectrum. Manganese may exhibit vibrational modes in the mid-infrared region, depending on its oxidation state and coordination environment.

3.3. Photoluminescence studies

Photoluminescence spectroscopy played a pivotal role in uncovering the optical properties of the material. Photoluminescence excitation (PLE) and photoluminescence (PL) spectra $Ca_3La_2W_2O_{12}$:$x$$Mn^{4+}$ phosphors are shown in Fig. 4. The spectral measurements were conducted under standard room temperature conditions. Prior studies have

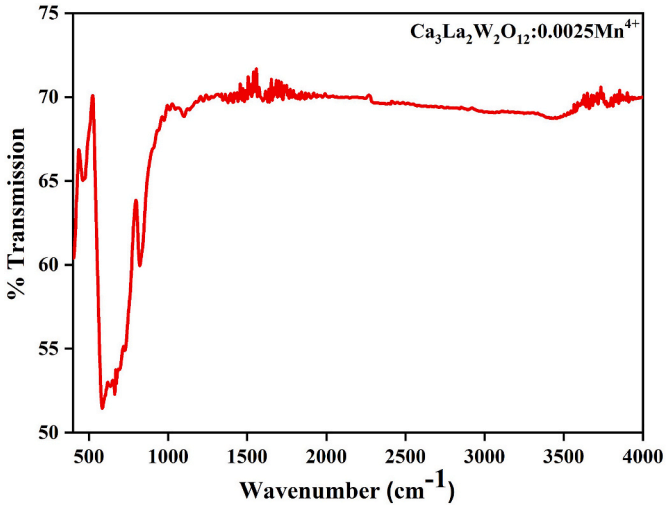

Fig. 3. FT-IR spectrum of the $Ca_3La_2W_2O_{12}$:0.0025Mn^{4+} phosphor.

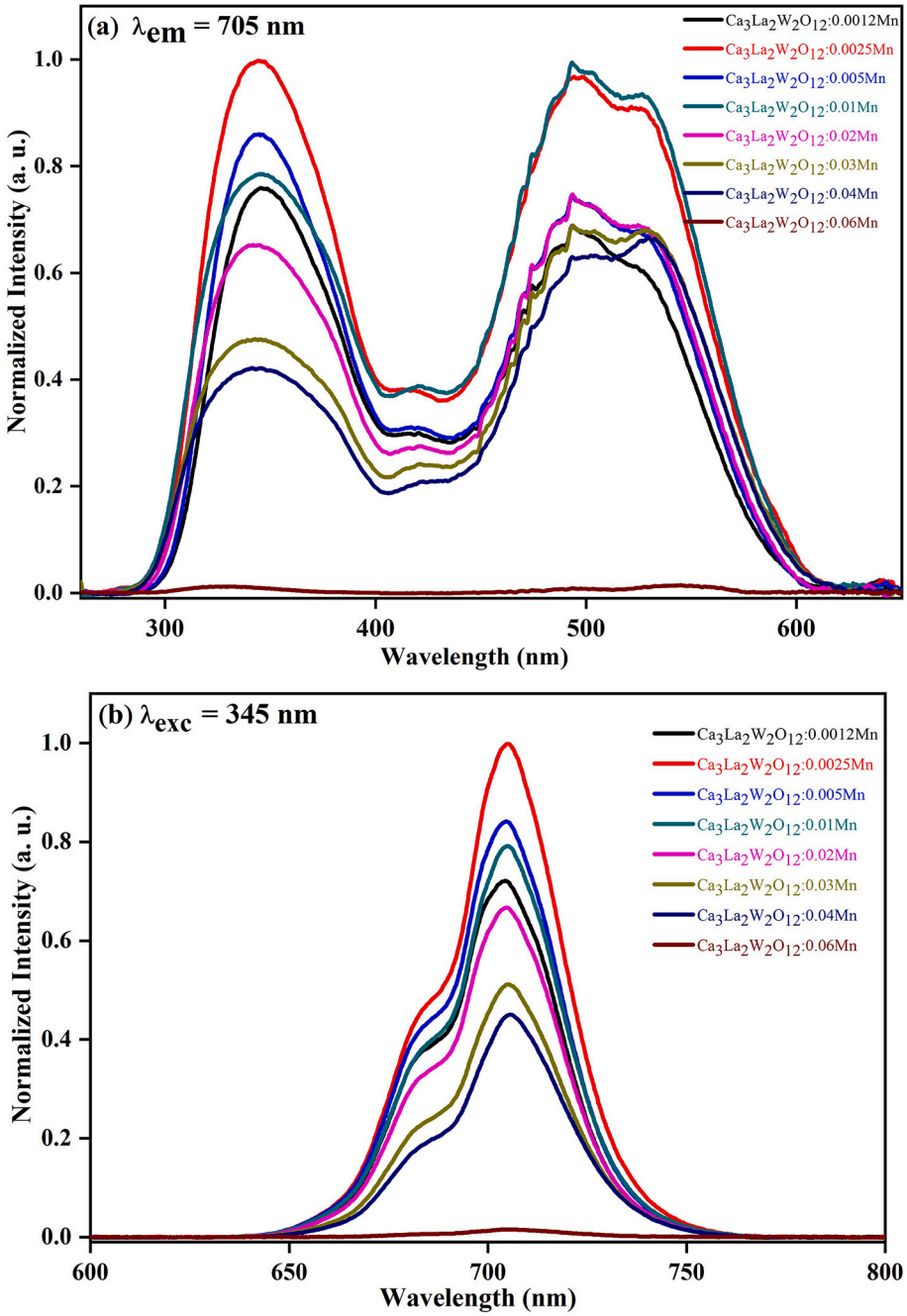

Fig. 4. (a) Photoluminescence excitation (PLE) spectra measured at λ_{em} = 705 nm, and (b) Photoluminescence emission (PL) spectra measured at λ_{exc} = 345 nm.

established distinct photoluminescence (PL) characteristics associated with different oxidation states of manganese ions. Specifically, Mn^{2+} ions exhibit PL emissions within the spectral range of 450–610 nm, whereas Mn^{4+} ions are known to produce PL emissions in the extended range of 610–790 nm. In contrast, Mn^{3+}, Mn^{5+}, and Mn^{6+} ions exhibit PL emissions in the near-infrared region. Notably, Mn^{7+} ions have been observed to be non-emissive [42–44]. Consequently, the data presented in the figure affirm that the observed photoluminescence (PL) and photoluminescence excitation (PLE) properties are attributed to the presence of Mn^{4+} metal ions within the composition of the phosphors.

The PLE spectra for the phosphors were recorded by monitoring the far red emission at 705 nm, as shown in Fig. 4 (a). Two significant wide bands were discovered in the ultraviolet to visible spectral region. The band at 345 nm would be attributed to the mixing of a charge-transfer band (CTB) due to Mn^{4+}-O^{2-} interaction and the $^4A_2 \rightarrow {}^4T_1$ transition bands in the Mn^{4+} center. On the other hand, the PLE peak at 500 nm was attributed to the $^4A_2 \rightarrow {}^4T_2$ transition of Mn^{4+} ion [7,11,45]. In addition, the intensity of the PLE spectra was contingent upon the concentration of Mn^{4+}. Both peaks displayed their highest intensity when x = 0.0025 mol concentration. It is worth noting that these predominant excitations corresponded to the emissions of near-ultraviolet or visible light-emitting device chips. Prepared phosphors exhibit significant absorption in both UV and visible light bands, and their emission spectra significantly appeared in the far red lighting group. Consequently, this phosphor can be utilized in indoor plant-growing LEDs.

Fig. 4 (b) reveals PL emission spectra of the $Ca_3La_2W_2O_{12}$:$x$$Mn^{4+}$ phosphors at the excited wavelength of λ_{exc} = 345 nm. The peak was observed at 705 nm which was due to $^2E_g \rightarrow {}^4A_2$ transition [46,47]. The position or the location of the peak was consistent with increasing Mn^{4+}

doping concentration. However, the intensity of the prominent peak varies significantly with increasing Mn^{4+} doping concentration. The maximum intensity of the prepared phosphors was observed for the doping concentration $x = 0.0025$, and the photoluminescence intensity decreases with further increase of Mn^{4+} doping concentration. The decrease in photoluminescence intensity after $x = 0.0025$ concentration was due to the concentration quenching phenomenon of Mn^{4+} ions. It was observed that at lower concentration of Mn^{4+} ions, the photoluminescence intensity increased with increasing concentration of Mn^{4+} of luminescent centers and reached saturation at $x = 0.0025$. The observed phenomenon can be attributed to an increase in the intensity of luminescent centers within the material. This increased concentration of luminescent centers results in a reduction of the average distance between adjacent Mn^{4+} ions. Consequently, this proximity enhances the likelihood of non-radiative interactions between Mn^{4+} ions, significantly elevating the occurrence of such interactions with increasing ion concentration. Consequently, these non-radiative processes contribute to the quenching of fluorescence within the phosphor, ultimately leading to a decrease in photoluminescence intensity. In this context, it is reasonable to propose that the introduction of Mn^{4+} ions result in their incorporation at metal sites within the $Ca_3La_2W_2O_{12}$ host matrix. This substitution of Mn^{4+} ions for other metal ions in the host matrix is indicative of a mechanism that generates oxygen vacancies, thereby introducing negative charges to the lattice. These negative vacancies affect the photoluminescence intensity leading to the transfer of energy from luminescent activators to the vacancies in the host matrix. The observed concentration quenching phenomenon suggests the presence of a non-radiative energy degeneracy process affecting the excited Mn^{4+} ions. The high doping concentration of Mn^{4+} ions lead to an increase in non-radiative energy transitions, causing a higher level of energy loss. This is directly linked to the elevated concentration of Mn^{4+} ions in the material, resulting in a decrease in radiative emissions. Currently, research on red phosphors is primarily centered on phosphors doped with rare earth ions. However, these rare earth ions are often prohibitively expensive. This study explores the use of Mn^{4+} instead of Eu^{3+} or Sm^{3+} to reduce costs, as Mn^{4+} offers excellent luminous characteristics at a lower price. Additionally, it should be noted that the lower concentration of Mn^{4+} ions in the investigated host material makes it a more economically feasible phosphor option. It has been well established that the far red color of the ion is very useful for effective in the photo-morphogenetic needs of plants. Mn^{4+}-doped $Ca_3La_2W_2O_{12}$ phosphor produces far red light, making it a great alternative to the far red light needed for plant development. Further the present results, though preliminary in nature, suggest that Mn^{4+}-doped $Ca_3La_2W_2O_{12}$ phosphor have potential to serve as excellent candidates that can be used as a potential phosphor being applied for plant growth. On a similar note, Liang et al. [48] studied $KLaMgWO_6$:Mn phosphor, which emitted in the far red region with a peak at 696 nm. They also fabricated LEDs by combining the phosphor with 365 nm LED chips, suggesting that the phosphors could be applicable for artificial plant cultivation. Similarly, Liu et al. [49] synthesized deep red-emitting Mg_2InSbO_6:Mn phosphor, which showed emission at 665 nm due to the usual Mn^{4+} transition. The emission of fabricated LEDs with this phosphor showed that the emission spectra completely overlapped with the plant pigments' absorption spectra, suggesting that these samples could be applicable for artificial plant cultivation. Upon comparing the emission and excitation spectra of our studied samples with those in published papers, it seems that our samples may be suitable for artificial plant cultivation. However, further in-depth study is necessary to reach a definitive conclusion.

The Dexter theory suggests that the energy transfer is happened due to electric multipolar interactions in which the photoluminescent intensity (I) and the dopant concentration can be given as [50,51].

$$ {}^{I}/_{x} = K\left[1 + \chi(x)^{\gamma/3}\right]^{-1} \quad (2) $$

Here, γ is the multipolar interactions constant equal to 6, 8 or 10 corresponding to dipole-dipole, dipole-quadrupole and quadrupole-quadrupole interactions respectively between neighboring ions. Additionally, K and χ denote the interaction constants [7,50]. To maintain consistency with the prescribed interaction constants, all emission data were acquired under the same excitation wavelength, specifically at 345 nm. In Fig. 5 (b), a logarithmic plot of $\log(I/x)$ versus $\log(x)$ is presented for $Ca_3La_2W_2O_{12}$:$x$$Mn^{4+}$ phosphors, focusing on the prominent emission peaks occurring at 705 nm. The estimated γ values are notably closer to 8, which strongly suggests the preeminence of dipole-quadrupole interactions as the governing factor in this effect. Importantly, this finding corroborates prior research conducted on similar phosphors [7,47,50].

3.4. Crystal field analysis

When Mn^{4+} ions are excited by ultraviolet light, they show the transition from $^4A_{2g}$ ground state to the $^4T_{1g}$ and $^4T_{2g}$ excited states. Subsequently, a non-radiative transition occurs, leading to the lowest excited state ^2E_g. Eventually, the electrons undergo a radiative transition from ^2E_g to the $^4A_{2g}$ ground state, resulting in far red emissions. The crystal field strength parameter Dq can be estimated using the equation.

$$ Dq = E\left({}^4A_2 \rightarrow {}^4T_2\right)/10 \quad (3) $$

Other crystal field parameters (termed as Racah parameters) B and C can be evaluated as follows:

$$ \frac{Dq}{B} = \frac{15(x-8)}{x^2 - 10x} \quad (4) $$

The crystal field strength parameter Dq, along with Racah parameters B and C, can be estimated using specific methodologies outlined in Refs. [52–54].

$$ x = E\left({}^4A_2 \rightarrow {}^4T_1\right) - E\left({}^4A_2 \rightarrow {}^4T_2\right) / Dq \quad (5) $$

$$ \frac{E\left({}^2E \rightarrow {}^4A_2\right)}{B} = \frac{3.05C}{B} - \frac{1.8C}{Dq} + 7.9 \quad (6) $$

The literature suggests that a Dq/B ratio exceeding 2.2 signifies a strong crystal field. In this context, Mn^{4+} exhibits the lowest excited state as ^2E_g within a robust crystal field system. This results in narrow band emissions attributed to the spin-forbidden transition from ^2E_g to $^4A_{2g}$. In the prepared series of samples, consistent peak positions across the spectra indicate that calculated values are likely similar for all samples. Based on the emission and excitation spectra of $Ca_3La_2W_2O_{12}$:$x$$Mn^{4+}$, specific energy values for transitions E($^4A_{2g} \rightarrow {}^4T_{1g}$), E($^4A_{2g} \rightarrow {}^4T_{2g}$), and E($^2E_g \rightarrow {}^4A_{2g}$) are determined as 27322 cm^{-1}, 19762 cm^{-1}, and 14204 cm^{-1}, respectively. The estimated values for Dq, B, and C for $Ca_3La_2W_2O_{12}$:$x$$Mn^{4+}$ are 1976 cm^{-1}, 745 cm^{-1}, and 2892 cm^{-1}, respectively. The calculated Dq/B ratio of 2.65 suggests that Mn^{4+} is situated in a strong crystal field. Interestingly, the energy difference between ^2E_g and $^4A_{2g}$ seems to be influenced more by the nephelauxetic effect than by the crystal field strength itself.

$$ \beta = \sqrt{\left(\frac{B}{B_0}\right)^2 + \left(\frac{C}{C_0}\right)^2} \quad (7) $$

Here, B_0 and C_0 are Racah parameters and have fixed values. The nephelauxetic parameter, estimated using references indicates β value of 0.929 for the prepared sample [53–55]. This value suggests that the covalency degree between Mn^{4+} and O^{2-} is low compared to other systems like $SrTiO_3$:Mn^{4+} and $BaLaLiTe_{1-x}O_6$:xMn [53,56].

3.5. CIE analysis

Fig. 6 shows the Commission Internationale de L'Eclairage (CIE) coordinates for $Ca_3La_2W_2O_{12}$:0.0025Mn^{4+} phosphor which was

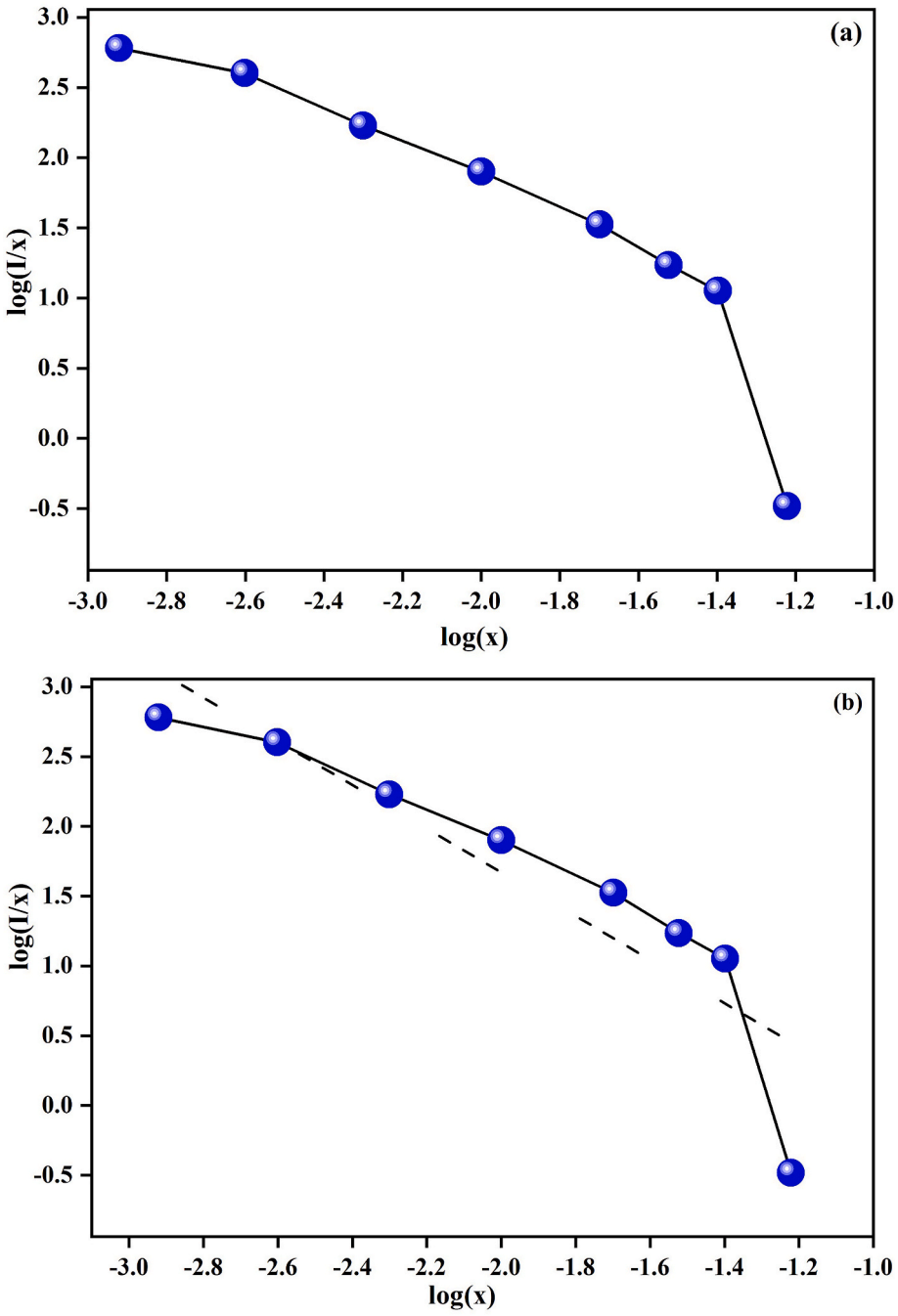

Fig. 5. (a) Variation in the emission intensity of strong emission (705 nm) as a function of Mn^{4+} concentration and (b) log(I/x) vs log(x) plot to estimate the θ value.

obtained using the PL spectra. The coordinates in Table 2 were found to be in the deep-red region of the color spectrum with very high color purity while using the standard illumination lamp (A). To validate this observation, a comprehensive verification process was undertaken by capturing digital images of the identical phosphor under both natural daylight and ultraviolet (UV) light conditions with a 365 nm excitation source. As illustrated in Fig. 7, the image acquired under natural daylight conditions (Fig. 7 (a)) exhibited a distinct light red coloration. In severe contrast, the image captured under 365 nm UV excitation (Fig. 7 (b)) exposed the substance as a red powder, further confirming the deep-red appearance. This empirical evidence provides robust support for the previously estimated coordinates and the inherent deep-red characteristic of the phosphor under investigation. The correlated color temperature (CCT) of the phosphor can be estimated using equation [30, 57]:

$$CCT = -\ 437n^3 + 3601n^2 - 6861n + 5514.31 \quad (8)$$

Here, $n = (x - x_e)/(y - y_e)$ and x_e is equal to 0.3320 and y_e is equal to 0.1858. The estimated CCT value for the phosphors is mentioned in Table 2, which suggests the phosphor is suitable for a work environment where a red illumination is needed.

3.6. EPR studies

An investigation has been carried out to detect the presence of Mn^{4+} ions in $Ca_3La_2W_2O_{12}$ phosphor using the technique of EPR, and is shown in Fig. 8. Fig. 8 clearly shows that the two signals are observed for all samples, one at nearly 1500 Gauss and the other at 3000 Gauss. Also, the

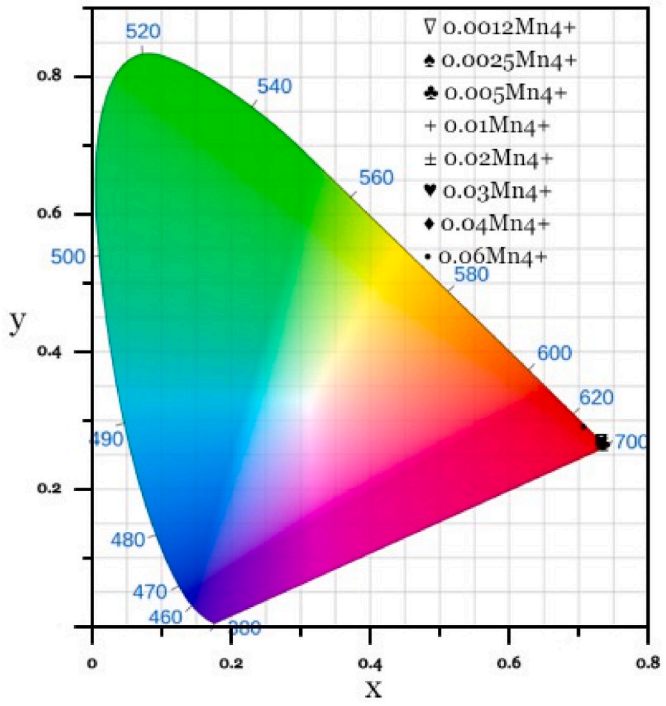

Fig. 6. CIE chromaticity diagram for $Ca_3La_2W_2O_{12}$:xMn^{4+} (x: 0.0012–0.06) phosphor (λ_{exc} = 345 nm).

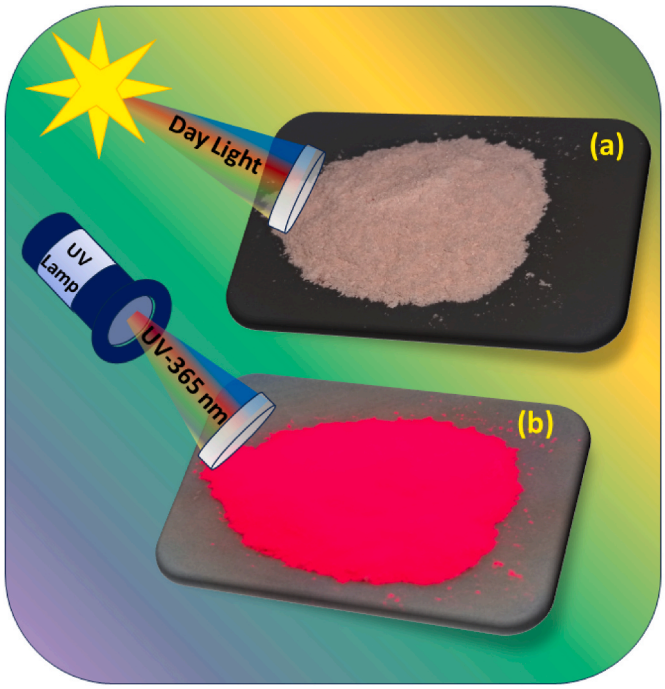

Fig. 7. Digital images of $Ca_3La_2W_2O_{12}$:0.0025Mn^{4+} phosphor under a room light and (b) under UV 365 nm.

Table 2
CIE chromaticity coordinates and correlated color temperature (CCT) of $Ca_3La_2W_2O_{12}$:xMn^{4+} (x: 0.0012–0.06) phosphor.

S. No.	Sample Composition	*x*	*y*	*Color purity (%)*	*CCT (K)*
1	$Ca_3La_2W_2O_{12}$:0.0012Mn	0.732	0.268	99.22	7046
2	$Ca_3La_2W_2O_{12}$:0.0025Mn	0.732	0.268	99.22	6974
3	$Ca_3La_2W_2O_{12}$:0.005Mn	0.734	0.266	99.74	6641
4	$Ca_3La_2W_2O_{12}$:0.01Mn	0.732	0.268	99.22	7101
5	$Ca_3La_2W_2O_{12}$:0.02Mn	0.732	0.268	99.22	6977
6	$Ca_3La_2W_2O_{12}$:0.03Mn	0.732	0.268	99.22	6982
7	$Ca_3La_2W_2O_{12}$:0.04Mn	0.734	0.266	99.74	5838
8	$Ca_3La_2W_2O_{12}$:0.06Mn	0.710	0.290	93.64	7158

intensities of the EPR signals are increased with increasing Mn^{4+} concentration. To have a better understanding of the EPR results we compare the samples with the lowest Mn^{4+} (x = 0.0012) and highest Mn^{4+} (x = 0.06) concentration in the phosphor series, as shown in Fig. 9. The spectrum for 0.0012 mol of Mn^{4+} ion $Ca_3La_2W_2O_{12}$ phosphor is shown in Fig. 9 (a). The spectrum in the vicinity of g ~2.0 arises from two overlapping EPR lines. The first spectrum is characterized by six-lines with a g-value equal to 1.98. A hyperfine interaction of the electron with a nucleus with spin S = 5/2 results in the six-line spectrum. The estimated hyperfine splitting is about 63 Gauss. The individual lines of the six-line spectrum have a linewidth of about 58 Gauss that is estimated from a spectrum of the phosphor with 0.0012 mol of Mn^{4+} ion $Ca_3La_2W_2O_{12}$ phosphor. Apart from the lines in the free electron region, a low filed line is seen at g ~4.0.

It is hypothesized in the literature that the structure of $Ca_3La_2W_2O_{12}$ closely resembles that of $Ca_5Re_2O_{12}$ [58,59]. In $Ca_5Re_2O_{12}$, Ca atoms occupy four atomic sites. The Ca1 and Ca2 atoms have eight oxygen neighbors that are in irregular arrangements. On the other hand, Ca3 and Ca4 atoms have nine and six oxygen neighbors. There are three kinds of W^{6+} sites and there are six oxygen atoms around W^{6+} atoms in all the three sites. Mons et al. [58] indicate that the structure contains building elements, that may be described as derived from the perovskite

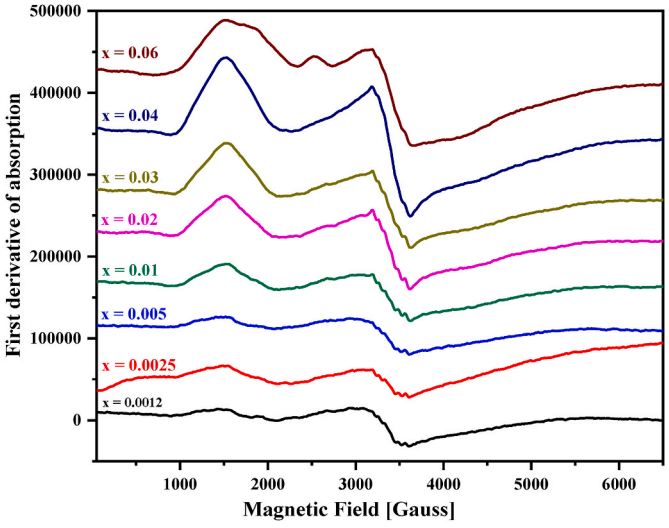

Fig. 8. EPR spectrum for $Ca_3La_2W_2O_{12}$:xMn^{4+} (x: 0.0012–0.06) phosphors.

structure, $CaTiO_3$.

It can be considered that the present experimental results indicate that Mn^{4+} ions are in a tetravalent state in the present system. Mn^{4+} ion has an ionic radius of 0.53 Å in a six-fold coordination [60]. Ca^{2+} ion (Ca1 and Ca2) has an ionic radius of 1.12 Å in eight-fold coordination and an ionic radius of 1.0 Å (Ca4) and 1.18 Å (Ca3) in six-fold and nine-fold coordination. La^{3+} ion (La1 and La2) has an ionic radius of 1.16 Å in an eight-fold coordination. In six-fold and nine-fold coordination, La^{3+} ion has an ionic radius of 1.032 Å and 1.216 Å respectively. On the other hand, W^{6+} has an ionic radius of 0.6 Å in a six-fold coordination. The Mn^{4+} ion, with an ionic radius of 0.53 Å, exhibits a preference for substituting W^{6+} ions in $Ca_3La_2W_2O_{12}$, as the ionic radius of W^{6+} is close to that of Mn^{4+} ion. Examples of Mn^{4+} doped systems, where the ion replaces cations with ionic radii similar to Mn^{4+}, include $Ba_3Y_2WO_9$ [61], $Cs_2WO_2F_4$ [62], Na_2SiF_6 [63], and $BaTiF_6$ [64].

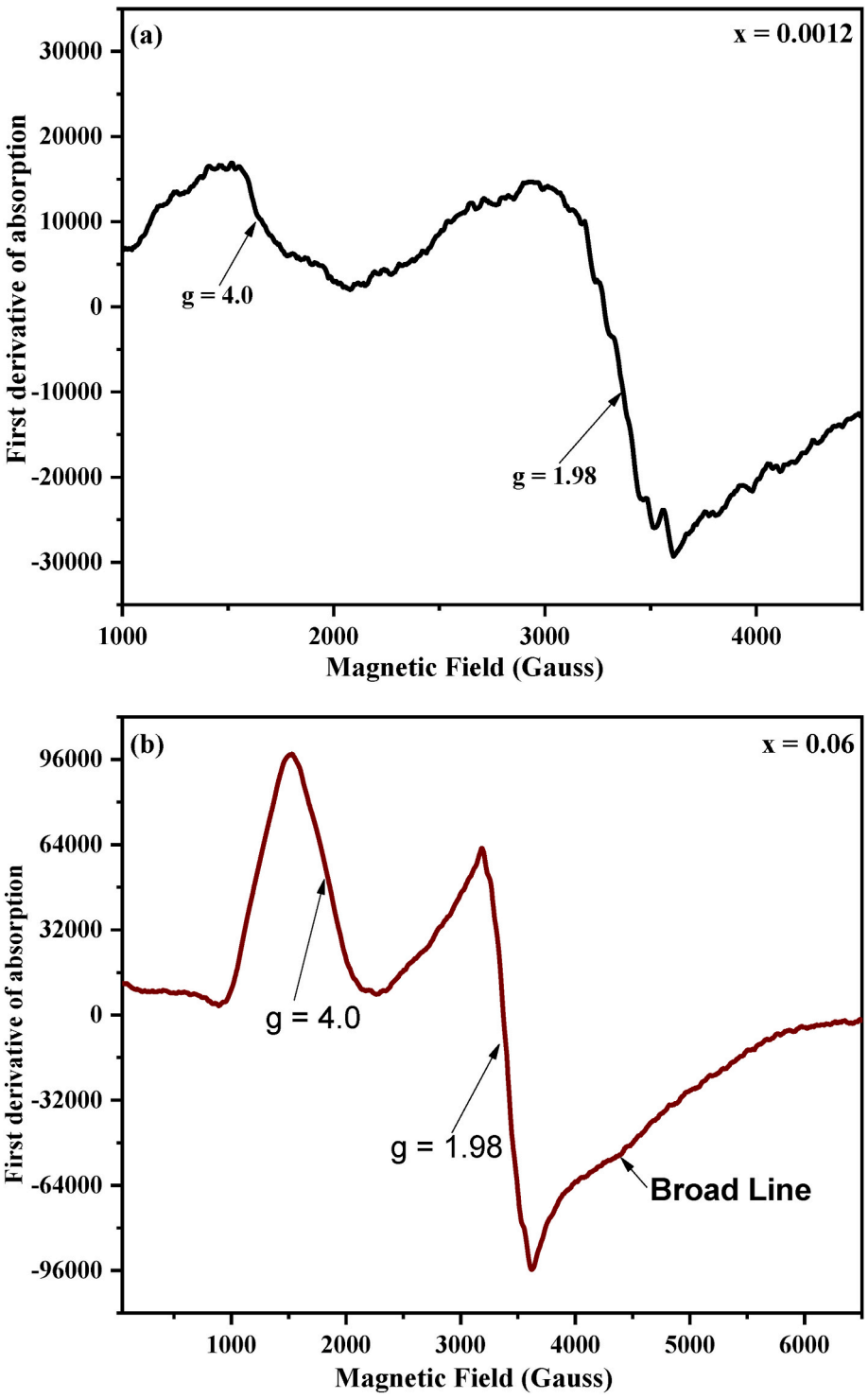

Fig. 9. Zoomed room temperature EPR spectrum of (a) 0.0012 mol and (b) 0.06 mol concentration of Mn^{4+} doped $Ca_3La_2W_2O_{12}$ phosphor.

In general, Mn ions can exist in three possible valence states viz., Mn^{2+}, Mn^{3+}, and Mn^{4+}. In a study on Mn doped $SrTiO_3$, Müller [60] has argued that the observed resonance is not due to Mn^{2+} ion on the basis of *g*-values. The observed *g*-value for Mn ion in their system is below 2.0 and is equal to 1.994. Further, the relaxation time of Mn^{3+} ion is expected to be so short that no resonance is observable at room temperature. Müller points out that Mn^{3+} ion is isoelectronic to Cr^{2+} and no resonance has been observed for Cr^{2+} ion in MgO system by Wertz et al. [65,66]. Müller [60] concludes that the observed resonance in $SrTiO_3$: Mn can come from $\Delta M_S = \pm 1$ transitions of the tetravalent Mn ion (Mn^{4+}, $3d^3$) with spin = 3/2 at Ti^{4+} position in $SrTiO_3$. Based on these arguments, it is speculated that the observed signals in $Ca_3La_2W_2O_{12}$: Mn^{4+} are due to Mn^{4+} ions located at W^{6+} sites. These explanations are consistent with the observed luminescence results which strongly suggest that the Mn ions in the $Ca_3La_2W_2O_{12}$ system are in Mn^{4+} state. Due to this state of Mn^{4+} ion, the synthesized systems generated red-deep emission at far-red region with a prominent peak at 705 nm when located at octahedral sites.

In an octahedral anion crystal field, Mn^{4+} ion has a ground state corresponding to an orbital singlet, A_2. Consequently, the spin-lattice

relaxation is weak and this makes EPR of Mn^{4+} easy to observe even at high temperatures [65]. On the other hand, Mn^{3+} ion ($3d^4$ with S = 3/2) is unlikely to have an observable signal as it exhibits a large zero-field splitting and strong spin-lattice relaxation as the ground state of Mn^{3+} ion is the orbital doublet [67].

The observed six-lines (Fig. 9 (a)), though not clearly seen, are due to $\Delta M_I = 0$ and $\Delta M_S = \pm 1$ transitions typical of Mn^{4+} ion in a powder system. The lines are hyperfine lines arising due to the interaction of the electron with a nucleus with spin 5/2 (Mn^{4+} ion). The observation of the lines in $Ca_3La_2W_2O_{12}$ phosphor shows that Mn ions are incorporated in the lattice and the observed red luminescence shows that they are in a tetravalent state. The *g*-value (1.98) observed in the phosphor indicates that the ions are located in sites with nearly cubic symmetry [68].

Apart from the six-line spectrum, a low-intensity broad line overlaps the main spectrum (as shown in Fig. 9 (a)). At high dopant concentrations ($x = 0.06$), this broad line becomes more pronounced (Fig. 9 (b)). The estimated *g*-value is not accurate and is found to be about 1.82. The linewidth of the broad line is about 950 Gauss. It is speculated that the broad line is due to the Fe^{3+} ion present in the lattice as an impurity. This impurity can come from starting materials used in the preparation of the phosphor. In addition to these lines seen in the vicinity of $g \sim 2.0$, a low field line is observed at $g \sim 4.0$. This line is broad with a linewidth of about 577 Gauss. This line is also attributed to Fe^{3+} ion experiencing strong crystal fields and perhaps located at sites with distorted environment.

The present EPR study is on a sample of the phosphor that is in powder form. In this type of analysis, the spectrum's anisotropies are averaged out, making it difficult to discern finer details. Crystal structure data reveals three types of octahedral sites for the W^{6+} ion. Despite the substitution of Mn^{4+} ions for W^{6+} ions in $Ca_3La_2W_2O_{12}$, the EPR spectrum fails to display features indicative of Mn^{4+} ions in multiple sites. Li et al. [69] studied Nd^{3+} doped $Ca_3La_2W_2O_{12}$ co-doped with Mn^{4+} and Yb^{3+} ions, observing an asymmetric and slightly broad red emission band peaking at 709 nm for Mn^{4+} singly doped $Ca_3La_2W_2O_{12}$. However, this emission band does not signify the presence of Mn^{4+} ions in the three W^{6+} sites. In a separate investigation by Hirrle et al. [70] involving Mn, Nd, and Yb-doped $Ca_3La_2W_2O_{12}$ phosphor, Mn^{4+} emission around 700 nm was observed. The emitted line, broad and lacking distinctive features, couldn't be attributed to Mn^{4+} ions in three distinct W^{6+} sites. In the current study, the luminescence band similarly fails to exhibit characteristics indicative of Mn^{4+} ions in multiple sites.

It has been possible to simulate the EPR spectrum using the parameters derived from the observed spectrum. The simulated spectrum is shown in Fig. 10 and the parameters are taken from the 0.005 mol Mn^{4+} in $Ca_3La_2W_2O_{12}$ phosphor (as shown in Fig. 10 (a)). The simulated Fe^{3+} ion spectrum is superposed over the simulated Mn^{4+} spectrum, as shown in Fig. 10 (b). For the Mn^{4+} ion, the parameters $g = 1.98$ and $A = 63$ Gauss along with 55 Gauss for the individual linewidth are used in the simulation, as shown in Fig. 10 (c). The parameters $g = 1.82$ and a linewidth of 950 Gauss are utilized for the Fe^{3+} spectrum simulation, as shown in Fig. 10 (d). It is observed that the match between the experimental and simulated spectrum is reasonable.

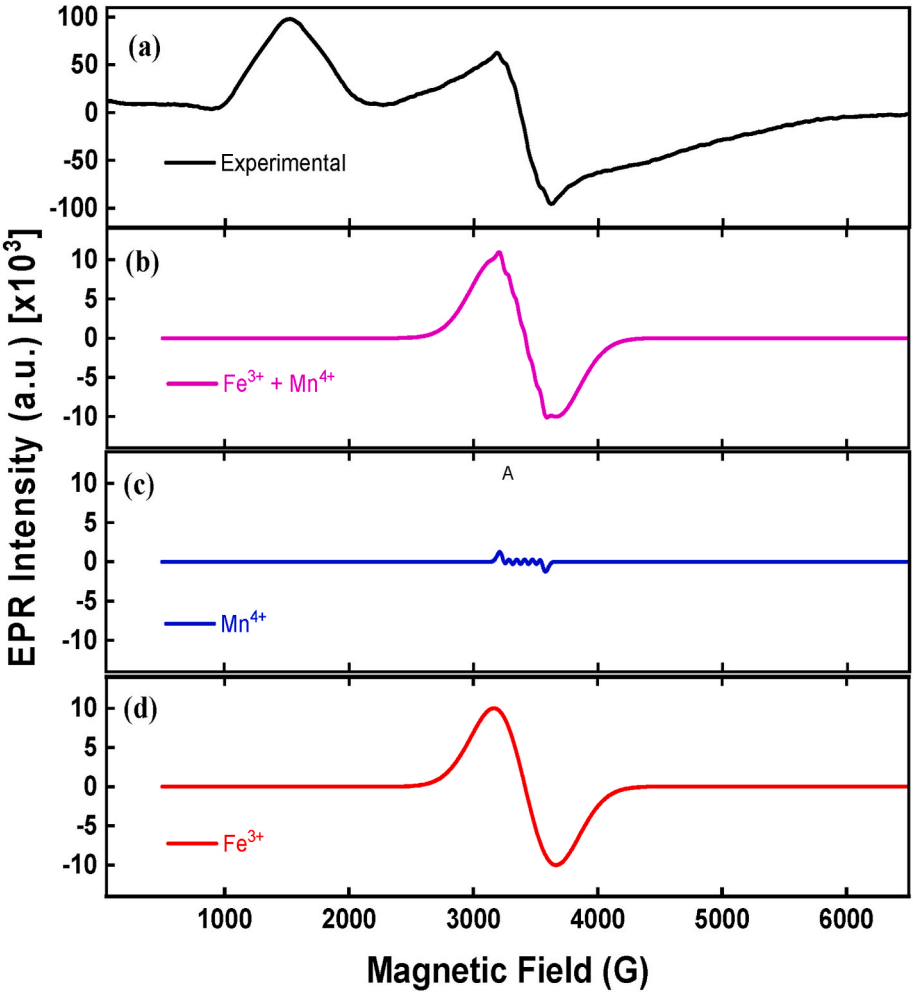

Fig. 10. (a) Room temperature EPR spectrum observed from x = 0.005 mol Mn^{4+} doped $Ca_3La_2W_2O_{12}$ phosphor, (b) simulated spectrum with contributions from Mn^{4+} and Fe^{3+} ions, (c) simulated spectrum only from Mn^{4+} ion and (d) simulated spectrum from Fe^{3+} ion.

4. Conclusions

It has been possible to successfully synthesize a series of highly efficient far red emitting phosphors with the formula $Ca_3La_2W_2O_{12}$:$x$$Mn^{4+}$, employing the sol-gel method. The synthesized samples exhibited a strikingly close resemblance to the JCPDS file No. 49–0965, confirming that the materials possessed a hexagonal structure with a space symmetry of $R\bar{3}m$. Our investigation also delved into the photoluminescence excitation (PLE) spectra, which unequivocally affirmed the existence of a Mn^{4+}-O^{2-} charge transfer band. Further spectral analysis revealed the presence of combined peaks associated with the $^4A_2 \rightarrow {}^4T_1$ and $^4A_2 \rightarrow {}^4T_2$ transitions of Mn^{4+} ions. Notably, we observed an emission peak at 705 nm, attributed to the $^2E_g \rightarrow {}^4A_{2g}$ transition of Mn^{4+} ions. Importantly, the maximum intensity of this emission was discerned at a doping concentration of x = 0.0025 mol for Mn^{4+} ions. Subsequently, at higher concentrations, we observed concentration quenching, a phenomenon attributed to dipole-quadrupole interactions within these samples. Our findings were effectively explained within the framework of the Dexter theory, shedding light on the underlying mechanisms responsible for these intricate energy transfer processes. The EPR lines detected in the $Ca_3La_2W_2O_{12}$:$x$$Mn^{4+}$ phosphor spectrum were identified as originating from Mn^{4+} ions. This observation consistently correlated with the observed red luminescence. Collectively, these findings provide compelling evidence for the presence of Mn^{4+} ions within the $Ca_3La_2W_2O_{12}$ lattice, specifically occupying W^{6+} sites. This work not only advances our understanding of the luminescent properties of Mn-doped phosphors but also underscores their potential for various optoelectronic applications. The initial investigation suggests that this far red emitting phosphor could be utilized as a dual-responsive candidate in the use of ultraviolet and visible light-excited LEDs to boost plant development.

Declaration of competing interest

The authors declare that they have no known competing financial interests or personal relationships that could have appeared to influence the work reported in this paper.

Acknowledgements

This work was supported by Konkuk University in 2022.

References

[1] B. Del Rosal, E. Ximendes, U. Rocha, D. Jaque, In vivo luminescence nanothermometry: from materials to applications, Adv. Opt. Mater. 5 (2017) 1600508.
[2] C. Feldmann, T. Jüstel, C.R. Ronda, P.J. Schmidt, Inorganic luminescent materials: 100 years of research and application, Adv. Funct. Mater. 13 (2003) 511.
[3] A. Nande, A. Tiwari, S. Raut, R. Nayar, S.J. Dhoble, Luminescence nanomaterials for photocatalysis, in: B. Bhanvase, S. Sonawane, V. Pawade, A. Pandit (Eds.), Handbook of Nanomaterials for Wastewater Treatment, Elsevier, 2021, p. 209.
[4] L.A. DeWerd, C. Hammer, S. Kry, Medical applications of luminescent materials, in: Advances in Physics and Applications of Optically and Thermally Stimulated Luminescence, vol. 439, World Scientific, 2019.
[5] L. Chen, C.C. Lin, C.W. Yeh, R.S. Liu, Light converting inorganic phosphors for white light-emitting diodes, Materials 3 (2010) 2172.
[6] D. Chen, W. Xiang, X. Liang, J. Zhong, H. Yu, M. Ding, H. Lu, Z. Ji, Advances in transparent glass-ceramic phosphors for white light-emitting diodes-A review, J. Eur. Ceram. Soc. 35 (2015) 859.
[7] X. Huang, H. Guo, Finding a novel highly efficient Mn^{4+}-activated $Ca_3La_2W_2O_{12}$ far-red emitting phosphor with excellent responsiveness to phytochrome PFR: towards indoor plant cultivation application, Dyes Pigments 152 (2018) 36.
[8] J. Hu, T. Huang, Y. Zhang, B. Lu, H. Ye, B. Chen, H. Xia, C. Ji, Enhanced deep-red emission from Mn^{4+}/Mg^{2+} co-doped $CaGdAlO_4$ phosphors for plant cultivation, Dalton Trans. 48 (2019) 2455.
[9] L. Li, Y. Pan, Y. Huang, S. Huang, M. Wu, Dual-emissions with energy transfer from the phosphor $Ca_{14}Al_{10}Zn_6O_{35}$:Bi^{3+}, Eu^{3+} for application in agricultural lighting, J. Alloys Compd. 724 (2017) 735.
[10] J. Chen, C. Guo, Z. Yang, T. Li, J. Zhao, Li_2SrSiO_4:Ce^{3+}, Pr^{3+} phosphor with blue, red, and near-infrared emissions used for plant growth LED, J. Am. Ceram. Soc. 99 (2016) 218.
[11] Z. Zhou, J. Zheng, R. Shi, N. Zhang, J. Chen, R. Zhang, H. Suo, E.M. Goldys, C. Guo, Ab initio site occupancy and far-red emission of Mn^{4+} in cubic-phase La $(MgTi)_{1/2}O_3$ for plant cultivation, ACS Appl. Mater. Interfaces 9 (2017) 6177.
[12] L. Wang, Y.G. Liu, H. Yu, R. Mi, X. Bu, L. Mei, H. Ding, Far-red-emitting Mn^{4+}-doped $Ca_2GdZr_2Al_3O_{12}$ phosphors for growing indoor plants, J. Lumin. 251 (2022) 19132.
[13] M. Wu, H. Wei, X. Huang, Q. Liu, S. Duan, Y. Liu, R. Mi, X. Min, Z. Huang, W. Zhang, P. Cao, High-efficiency Ce^{3+} activated orthorhombic lanthanide silicate blue phosphors for plant growth lighting, Inorg. Chem. 62 (2023) 12793.
[14] D. Cozzolino, Advantages and limitations of using near infrared spectroscopy in plant phenomics applications, Comput. Electron. Agric. 212 (2023) 108078.
[15] W. Xu, X. Zhu, D. Zhao, L. Zheng, F. Shang, Z. Zhang, Optical thermometry based on near-infrared luminescence from phosphors mixture, J. Rare Earths 40 (2022) 201.
[16] G.S. Folli, L.P. Santos, F.D. Santos, P.H. Cunha, I.F. Schaffel, F.T. Borghi, I. H. Barros, A.A. Pires, A.V. Ribeiro, W. Romão, P.R. Filgueiras, Food analysis by portable NIR spectrometer, Food Chemistry Advances 1 (2022) 100074.
[17] R. Vitorino, A.S. Barros, S. Guedes, D.C. Caixeta, R. Sabino-Silva, Diagnostic and monitoring applications using near infrared (NIR) spectroscopy in cancer and other diseases, Photodiagnosis Photodyn. Ther. (2023) 103633.
[18] M. Wahby, M.K. Heinrich, D.N. Hofstadler, E. Neufeld, I. Kuksin, P. Zahadat, T. Schmickl, P. Ayres, H. Hamann, Autonomously shaping natural climbing plants: a bio-hybrid approach, R. Soc. Open Sci. 5 (2018) 180296.
[19] J. Xiang, J. Chen, N. Zhang, H. Yao, C. Guo, Far red and near infrared double-wavelength emitting phosphor Gd_2ZnTiO_6:Mn^{4+}, Yb^{3+} for plant cultivation LEDs, Dyes Pigments 154 (2018) 257.
[20] S. Miao, R. Shi, Y. Zhang, D. Chen, Y. Liang, Deep-red $Ca_3Al_2Ge_3O_{12}$:Eu^{3+} garnet phosphor with near-unity internal quantum efficiency and high thermal stability for plant growth application, Advanced Materials Technologies (2023) 2202103.
[21] S. Gu, M. Xia, C. Zhou, Z. Kong, M.S. Molokeev, L. Liu, W.Y. Wong, Z. Zhou, Red shift properties, crystal field theory and nephelauxetic effect on Mn^{4+}-doped $SrMgAl_{10-y}Ga_yO_{17}$ red phosphor for plant growth LED light, Chem. Eng. J. 396 (2020) 125208.
[22] H. Chen, H. Lin, Q. Huang, F. Huang, J. Xu, B. Wang, Z. Lin, J. Zhou, Y. Wang, A novel double-perovskite Gd_2ZnTiO_6:Mn^{4+} red phosphor for UV-based w-LEDs: structure and luminescence properties, J. Mater. Chem. C 4 (2016) 2374.
[23] J. Xiang, J. Chen, N. Zhang, H. Yao, C. Guo, Far red and near infrared double-wavelength emitting phosphor Gd_2ZnTiO_6:Mn^{4+}, Yb^{3+} for plant cultivation LEDs, Dyes Pigments 154 (2018) 257.
[24] L. Sun, B. Devakumar, J. Liang, B. Li, S. Wang, Q. Sun, H. Guo, X. Huang, Thermally stable La_2LiSbO_6:Mn^{4+}, Mg^{2+} far-red emitting phosphors with over 90% internal quantum efficiency for plant growth LEDs, RSC Adv. 8 (2018) 31835.
[25] Z. Tang, L. Jiang, J. Yang, J. Tang, A. Wu, Eu^{3+}-activated alkali rare-earth double-tungstate nanoparticles for near-ultraviolet-light-triggered indoor illumination, ACS Appl. Nano Mater. 5 (2022) 9072.
[26] Y. Yang, F. Li, Y. Lu, Y. Du, L. Wang, S. Chen, X. Ouyang, Y. Li, L. Zhao, J. Zhao, B. Deng, $CaGdSbWO_8$:Sm^{3+}: a deep-red tungstate phosphor with excellent thermal stability for horticultural and white lighting applications, J. Lumin. 251 (2022) 119234.
[27] Z. Li, X. Peng, L. Xu, G. Cao, Z. Jiang, B. Deng, Research on a new Tm^{3+}-doped $Ca_3La_2W_2O_{12}$ blue-emitting phosphor for plant-cultivation LEDs, in: 2022 International Conference on Optoelectronic Information and Functional Materials, vol. 12255, 2022, p. 469.
[28] L.X. Lovisa, D.F. Dos Santos, A.A.G. Santiago, M. Siu Li, E. Longo, F.V. Motta, M.R. D. Bomio, Enhanced red emission in $Sr_{1-x}Eu_xMo_{0.5}W_{0.5}O_4$ (x= 0.01, 0.02, 0.04) phosphor and spectroscopic analysis for display applications, J. Mater. Sci. 57 (2022) 8634.
[29] L. Zhang, B. Deng, S. Shu, Y. Wang, H. Geng, R. Yu, Preparation, characterization, and luminescence properties of $BiLaWO_6$:Eu^{3+} red-emitting phosphors for w-LEDs, Spectrochim. Acta Mol. Biomol. Spectrosc. 224 (2020) 117454.
[30] X. Wu, L. Du, Q. Ren, O. Hai, A far-red emission $Ca_3La_2W_2O_{12}$:xMn^{4+} phosphor for potential application in plant growth LEDs, J. Lumin. 249 (2022) 118993.
[31] J. Hou, W. Yin, L. Dong, Y. Li, Y. Liu, Z. Liu, G. Zhao, G. Zhang, Y. Fang, A novel red-emitting Na_2NbOF_5:Mn^{4+} phosphor with ultrahigh color purity for warm white lighting and wide-gamut backlight displays, Materials 14 (2021) 5317.
[32] A.A. Bhat, S.A. Khandy, A.M. Ali, R. Tomar, Photoluminescence emission studies on a lanthanum-doped lead free double halide perovskite, La:Cs_2SnCl_6, J. Phys. Chem. Lett. 14 (2023) 5004.
[33] A.A. Bhat, M.B. Zaman, J.H. Malik, K.A. Malik, I. Assadullah, R. Tomar, Facile way of making hydrothermally synthesized crystalline $SrSnO_3$ perovskite nanorods suitable for blue LEDs and spintronic applications, ACS Omega 6 (2021) 16356.
[34] V. Singh, J.K. Lee, M. Seshadri, A.A. Bhat, S. Watanabe, T.G. Rao, Photoluminescence and EPR spectroscopic studies on narrowband ultraviolet-B (NB-UVB) emitting trivalent gadolinium-doped $CaAl_4O_7$ material for phototherapy lamps, Ceram. Int. 50 (2024) 4632.
[35] N. Sharma, M. Deepa, P. Varshney, S.A. Agnihotry, FTIR and absorption edge studies on tungsten oxide based precursor materials synthesized by sol–gel technique, J. Non-Cryst. Solids 306 (2002) 129.
[36] H. Najafi-Ashtiani, A. Bahari, S. Gholipour, S. Hoseinzadeh, Structural, optical and electrical properties of WO_3–Ag nanocomposites for theelectro-optical devices, Appl. Phys. A 124 (2018) 1.
[37] A.A. El-Kheshen, F.H. El-Batal, UV-visible, infrared and Raman spectroscopic and thermal studies of tungsten doped lead borate glasses and the effect of ionizing gamma irradiation, Indian J. Pure Appl. Phys. 46 (2008) 225.

[38] A.A. Rabelo, M.C.D. Macedo, D.M.D.A. Melo, C.A. Paskocimas, A.E. Martinelli, R. M.D. Nascimento, Synthesis and characterization of $La_{1-x}Sr_xMnO_{3\pm\delta}$ powders obtained by the polymeric precursor route, Mater. Res. 14 (2011) 91.
[39] S. Gunasekaran, G. Anbalagan, Spectroscopic study of phase transitions in natural calcite mineral, Spectrochim. Acta Mol. Biomol. Spectrosc. 69 (2008) 1246.
[40] A.A. Bhat, I. Assadullah, A. Farooq, K.A. Malik, J.H. Malik, R. Tomar, S.A. Khandy, Band-gap alteration of Zn_2SnO_4 nanostructures for optical and photo-luminescent applications, Mater. Chem. Phys. (2023) 127993.
[41] A.A. Bhat, S.A. Khandy, I. Islam, R. Tomar, Optical, electrochemical and photocatalytic properties of cobalt doped $CsPbCl_3$ nanostructures: a one-pot synthesis approach, Sci. Rep. 11 (2021) 16473.
[42] R. Cao, J. Qiu, X. Yu, X. Sun, Spectroscopic investigation on $BaSO_4$:(Mn^{6+}, Mn^{5+}) crystal, ECS Journal of Solid State Science and Technology 2 (2013) 237.
[43] G. Blasse, B.C. Grabmaier, G. Blasse, B.C. Grabmaier, A General Introduction to Luminescent Materials, Springer Berlin Heidelberg, 1994, p. 1.
[44] R. Cao, Z. Shi, G. Quan, T. Chen, S. Guo, Z. Hu, P. Liu, Preparation and luminescence properties of Li_2MgZrO_4:Mn^{4+} red phosphor for plant growth, J. Lumin. 188 (2017) 577.
[45] R. Cao, X. Ceng, J. Huang, X. Xia, S. Guo, J. Fu, A double-perovskite Sr_2ZnWO_6:Mn^{4+} deep red phosphor: synthesis and luminescence properties, Ceram. Int. 42 (2016) 16817.
[46] R. Cao, Y. Zhao, Z. Hu, W. Shao, F. Xiao, G. Zheng, P. Liu, T. Chen, Synthesis and photoluminescence properties of $La(Mg_{1-x}Nb_x)O_3$:Mn^{4+} (x= 0.296 and 0.384) deep red-emitting phosphors, J. Lumin. 238 (2021) 118248.
[47] M. Gao, Y. Pan, Y. Jin, J. Lin, A review on the structural dependent optical properties and energy transfer of Mn^{4+} and multiple ion-codoped complex oxide phosphors, RSC Adv. 11 (2021) 760.
[48] J. Liang, B. Devakumar, L. Sun, Q. Sun, S. Wang, B. Li, X. Huang, Mn^{4+}-activated $KLaMgWO_6$: a new high-efficiency far-red phosphor for indoor plant growth LEDs, Ceram. Int. 45 (2019) 4564.
[49] Y. Liu, J. Gao, W. Shi, X. Feng, Z. Zhou, J. Wang, R. Yu, Deep-red-emitting Mg_2InSbO_6:Mn^{4+} phosphors with a double-perovskite structure for plant-cultivation LEDs: synthesis and photoluminescence properties, Ceram. Int. 47 (2021) 18814.
[50] X. Wu, L. Du, Q. Ren, O. Hai, A far-red emission $Ca_3La_2W_2O_{12}$:xMn^{4+} phosphor for potential application in plant growth LEDs, J. Lumin. 249 (2022) 118993.
[51] L. Shi, Y.J. Han, Z.G. Zhang, Z.X. Ji, D.C. Shi, X.Y. Geng, H. Zhang, M. Li, Z. W. Zhang, Synthesis and photoluminescence properties of novel Ca_2LaSbO_6:Mn^{4+} double perovskite phosphor for plant growth LEDs, Ceram. Int. 45 (2019) 4739.
[52] L. Shi, Y.J. Han, H.X. Wang, D.C. Shi, X.Y. Geng, Z.W. Zhang, High-efficiency and thermally stable far-red emission of Mn^{4+} in double cubic perovskite $Sr_9Y_2W_4O_{24}$ for plant cultivation, J. Lumin. 208 (2019) 307.
[53] W. Liu, D. Zhao, R.J. Zhang, L. Jia, L.N. Zhang, L.Y. Shi, A new series of long wavelength red phosphors $BaLaLiTe_{1-x}O_6$:xMn^{4+} for plant cultivation LED, Ceram. Int. 48 (2022) 10895.
[54] M.G. Brik, A.M. Srivastava, Electronic energy levels of the Mn^{4+} ion in the perovskite, $CaZrO_3$, ECS Journal of Solid State Science and Technology 2 (2013) R148.
[55] L. Qin, P. Cai, C. Chen, J. Wang, H.J. Seo, Synthesis, structure and optical performance of red-emitting phosphor Ba_5AlF_{13}:Mn^{4+}, RSC Adv. 7 (78) (2017) 49473–49479.
[56] Z. Bryknar, V. Trepakov, Z. Potůček, L. Jastrabık, Luminescence spectra of $SrTiO_3$:Mn^{4+}, J. Lumin. 87 (2000) 605–607.
[57] Y. Li, J. Chen, C. Chen, Tunable correlated color temperature of $NaSrPO_4$ phosphors via Dy^{3+} and Eu^{3+} co-doping for warm white light-emitting diodes, Optik 174 (2018) 1.
[58] H.A. Mons, M.S. Schriewer, W. Jeitschko, The crystal structures of the isotypic perrhenates $Ca_5Re_2O_{12}$ and $Sr_5Re_2O_{12}$, J. Solid State Chem. 99 (1992) 149.
[59] H.D. Autenrieth, S. Kemmler-Sack, W. Wischert, Lumineszenz und sensibilisierte emission der dreiwertigen seltenen erden in $Ca_3La_2W_2O_{12}$, Phys. Status Solidi 83 (1984) 631.
[60] K.A. Müller, Electron paramagnetic resonance of manganese IV in $SrTiO_3$, Phys. Rev. Lett. 2 (1959) 341.
[61] W. Wang, X. Yang, S. Xiao, $Ba_3Y_2WO_9$:Mn^{4+}: a near-UV and yellow-green light excited red phosphor for greenhouse cultivation, J. Lumin. 225 (2020) 117406.
[62] P. Cai, L. Qin, C. Chen, J. Wang, H.J. Seo, Luminescence, energy transfer and optical thermometry of a novel narrow red emitting phosphor: $Cs_2WO_2F_4$:Mn^{4+}, Dalton Trans. 46 (2017) 14331.
[63] H.D. Nguyen, C.C. Lin, M.H. Fang, R.S. Liu, Synthesis of Na_2SiF_6:Mn^{4+} red phosphors for white LED applications by co-precipitation, J. Mater. Chem. C 2 (2014) 10268.
[64] X. Gao, Y. Song, G. Liu, X. Dong, J. Wang, W. Yu, Narrow-band red emitting phosphor $BaTiF_6$:Mn^{4+}: preparation, characterization and application for warm white LED devices, Dalton Trans. 45 (44) (2016) 17886–17895.
[65] J.E. Wertz, P. Auzins, J.H.E. Griffiths, J.W. Orton, III Spin resonance studies of defects in magnesium oxide, Discuss. Faraday Soc. 28 (1959) 136.
[66] J.E. Wertz, P. Auzins, J.H.E. Griffiths, J.W. Orton, Electron transfers among transition elements in magnesium oxide, Discuss. Faraday Soc. 26 (1958) 66.
[67] A. Abragam, B. Bleaney, Electron Paramagnetic Resonance of Transition Ions, Clarendon P, 1970.
[68] D.M. Hofmann, A. Hofstaetter, U. Leib, B.K. Meyer, G. Counio, EPR and ENDOR investigations on CdS: Mn nanocrystals, J. Cryst. Growth 184 (1998) 383.
[69] K. Li, R. Van Deun, Enhancing the energy transfer from Mn^{4+} to Yb^{3+} via a Nd^{3+} bridge role in $Ca_3La_2W_2O_{12}$:Mn^{4+}, Nd^{3+}, Yb^{3+} phosphors for spectral conversion of c-Si solar cells, Dyes Pigments 162 (2019) 990.
[70] R. Hirrle, S. Kemmler-Sack, Energietransfer im System $Ca_3La_2W_2O_{12}$:Mn, Nd, Yb, Zeitschrift fur Naturforschung A 43 (1988) 81.